



HAL
open science

Controlling the force and the position of acoustic traps with a tunable acoustofluidic chip: Application to spheroid manipulations

Nathan Jeger-Madiot, Xavier Mousset, Chloé Dupuis, Lucile Rabiet, Mauricio Hoyos, Jean-Michel Peyrin, Jean-Luc Aider

► To cite this version:

Nathan Jeger-Madiot, Xavier Mousset, Chloé Dupuis, Lucile Rabiet, Mauricio Hoyos, et al.. Controlling the force and the position of acoustic traps with a tunable acoustofluidic chip: Application to spheroid manipulations. *Journal of the Acoustical Society of America*, 2022, 151 (6), pp.4165-4179. 10.1121/10.0011464 . hal-03832185v2

HAL Id: hal-03832185


<https://hal.science/hal-03832185v2>

Submitted on 27 Oct 2022

HAL is a multi-disciplinary open access archive for the deposit and dissemination of scientific research documents, whether they are published or not. The documents may come from teaching and research institutions in France or abroad, or from public or private research centers.

L'archive ouverte pluridisciplinaire **HAL**, est destinée au dépôt et à la diffusion de documents scientifiques de niveau recherche, publiés ou non, émanant des établissements d'enseignement et de recherche français ou étrangers, des laboratoires publics ou privés.

Controlling the force and the position of acoustic traps with a tunable acoustofluidic chip: Application to spheroid manipulations

Nathan Jeger-Madiot,^{1,a)}  Xavier Mousset,^{1,b)} Chloé Dupuis,^{1,b)} Lucile Rabiet,^{1,c)} Mauricio Hoyos,¹ Jean-Michel Peyrin,² and Jean-Luc Aider¹

¹Laboratoire de Physique et Mécanique des Milieux Hétérogènes, Unité Mixte de Recherche 7636 Centre National de la Recherche Scientifique, École Supérieure de Physique et de Chimie Industrielles de la Ville de Paris, Paris Sciences et Lettres University, Sorbonne Université, Université de Paris 1, Paris, 75005, France

²Sorbonne Universités, Faculté des Sciences et Ingénierie, CNRS UMR 8246, INSERM U1130, Neurosciences Paris Seine, Institut de Biologie Paris Seine, Paris, 75005, France

³Unité de Thérapie Cellulaire, APHP, Hôpital Saint-Louis, Université de Paris, Inserm U976 et CIC de Biothérapies CBT501, 75010 Paris, France

ABSTRACT:

A multi-node acoustofluidic chip working on a broadband spectrum and beyond the resonance is designed for cell manipulations. A simple one-dimensional (1D) multi-layer model is used to describe the stationary standing waves generated inside a cavity. The transmissions and reflections of the acoustic wave through the different layers and interfaces lead to the creation of pressure nodes away from the resonance condition. A transparent cavity and a broadband ultrasonic transducer allow the measurement of the acoustic energy over a wide frequency range using particle image velocimetry measurements and the relation between acoustic energy and the particles velocity. The automation of the setup allows the acquisition over a large spectrum with a high frequency definition. The results show a wide continuous operating range for the acoustofluidic chip, which compares well with the 1D model. The variation of the acoustic radiation force when varying the frequency can be compensated to ensure a constant amplitude for the ARF. This approach is finally applied to mesenchymal stem cell (MCS) spheroids cultured in acoustic levitation. The MSC spheroids can be moved and merged just by varying the acoustic frequency. This approach opens the path to various acoustic manipulations and to complex 3D tissue engineering in acoustic levitation. © 2022 Acoustical Society of America.

<https://doi.org/10.1121/10.0011464>

(Received 28 October 2021; revised 5 April 2022; accepted 7 May 2022; published online 23 June 2022)

[Editor: James F. Lynch]

Pages: 4165–4179

I. INTRODUCTION

The rise of microfluidics together with efficient piezoelectric devices during the last 20 years led to an increasing interest for acoustofluidics and its applications to acoustophoresis. These approaches have shown many benefits for soft, label-free, and non-contact manipulations of particles or biological cells in microfluidic systems (Laurell *et al.*, 2007; Wiklund, 2012). This rapidly growing research field addresses many challenges (Friend and Yeo, 2011; Wu *et al.*, 2019) in biotechnology, medicine, or chemistry. The main principles rely on the interaction between acoustic waves and the objects in suspension in a fluid. Depending

on the application, the acoustic forces can be combined with other forces like flow viscous drag (Pettersson *et al.*, 2007), optical (Dumy *et al.*, 2019), or gravity ones (Wiklund *et al.*, 2004). Acoustophoresis is used as a robust method for concentrating (Carugo *et al.*, 2014; Dron *et al.*, 2009; Nordin and Laurell, 2012), washing (Augustsson and Laurell, 2012), separating (Ding *et al.*, 2014; Pettersson *et al.*, 2007), or trapping (Evander and Nilsson, 2012; Jeger-Madiot *et al.*, 2021) cells. The most usual devices shape bulk acoustic waves (BAW) in order to obtain standing waves in a resonant micro-cavity or micro-channel (Hawkes and Coakley, 2001; Leshof *et al.*, 2012; Luo *et al.*, 2018).

Despite the relative simplicity of the principle, acoustophoresis may become challenging if accuracy (high selectivity for acoustic sorting, for instance), control, and/or performances (high throughput, for instance) are required by the targeted application.

The first key problem with such systems relies on the identification of the optimal resonance frequency peak and

^{a)}Electronic mail: nathan.jeger-madiot@espci.fr

^{b)}Also at: Sorbonne Universités, Faculté des Sciences et Ingénierie, CNRS UMR 8246, INSERM U1130, Neurosciences Paris Seine, Institut de Biologie Paris Seine, 75005 Paris, France.

^{c)}Also at: Unité de Thérapie Cellulaire, APHP, Hôpital Saint-Louis, Université de Paris, Inserm U976 et CIC de Biothérapies CBT501, 75010 Paris, France.

the estimation of the quality factor Q . It can be done with electrical methods like admittance curves (Dual and Schwarz, 2012) or differential impedance measurement (Vitali *et al.*, 2019). Others approaches used the static mechanic effects on the objects under levitation, such as the equilibrium with the gravitational forces (Hultström *et al.*, 2007), and the theoretical models (Settnes and Bruus, 2012) to estimate the acoustic pressure.

On the other hand, dynamic transient motions of the particles undergoing the acoustic waves are directly related to the acoustic pressure or energy which can then be inferred from the measurements of their velocities. The present issue consists of the assessment of the particle movement under the acoustic forces. Barnkob *et al.* (2010) developed a particle tracking method to measure the acoustic pressure. Hagsäter *et al.* (2007) and Augustsson *et al.* (2011) have used micro-particle image velocimetry (PIV) to characterize the acoustic properties of micro-channels and Dron and Aider (2012) proposed an optical method based on defocused particle images to evaluate the acoustic energy density inside the cavity.

Most of the acoustofluidics designs rely on the search of the best fit between the height of the cavity and the acoustic frequency, in order to maximize the ARF. Dron and Aider (2013) have shown that acoustofluidic systems still work beyond the resonant frequency, leading to the possibility to change the axial location of the acoustic levitation plane just by tuning the acoustic frequency. This was made possible because of the use of a broadband acoustic transducer and a multi-layer device, as suggested by Hill *et al.* (2002). The present work goes further and generalize the work of Dron and Aider (2013) to multi-node devices with a proper theoretical framework.

In this study, we focus on the design of a standing-wave cavity with several acoustic nodes. The geometry of the microfluidic chip and the broadband transducer allow the particles manipulation continuously over a large range of frequencies. The working setup is explained with a plain one-dimensional (1D) theoretical approach, which is validated by the measurement of the focusing particle velocities over a larger acoustic frequency spectrum. We show that the acoustic levitation is effective from 1.5 to 2.5 MHz. In our setup the trapped particles can be continuously moved from one axial position to another, in a stable way, just by changing the acoustic frequency.

To illustrate its potential, we applied this approach to human mesenchymal stem cells (hMSCs). After a first step, lasting ten hours, consisting in the aggregation and self-organization of the hMSCs into spheroids in acoustic levitation (Jeger-Madiot *et al.*, 2021), we were able to move the spheroids closer to each other in a stable way just by tuning the frequency, before finally merging them. This original approach opens the path to the scaffold-free creation and culture of assembloids and organoids of various cellular type, in acoustic levitation.

II. BACKGROUND THEORY

In this section, we first describe the basic theory of acoustics for a 1D model. From the knowledge of the acoustic field properties in the cavity, we can deduce the different forces acting on small particles or cells. All these properties will then be experimentally estimated using a μ PIV method.

A. Acoustic resonance in a multilayered device

In our system, the dimensions of the transducer d_{trans} and the cavity are very large in comparison to the wavelength ($d_{trans} = 8 \text{ mm} \gg \lambda_{2\text{MHz}} \approx 0,75 \text{ mm}$) so we can consider plane wave emission and reflection and we can use a 1D model to describe the wave emission, transmissions, and reflections through the different layers of the resonant cavity (Royer and Dieulesaint, 1999). Of course, it will only describe the axial component of the ARF, the transverse component being associated with radial gradient of the acoustic field which are not taken into account in this simple model.

The vibrating emitting surface is directly in contact with the suspending medium, i.e., there is no transmitting layer (of course the piezoelectric is isolated from the fluid by a quarter-wavelength layer). In the following, three layers are modeled: the water medium in which the particles are floating, the glass slide, opposite to the acoustic source, acting as the acoustic reflector and the semi-infinite medium, on the other side of the reflecting layer, modeled as a simple air layer (Fig. 1).

The classical equations of linear acoustics (Bruus, 2012b) can be applied in the material (n) considering an harmonic plane wave with the following parameters: the angular frequency $\omega = 2\pi f$, the wave number $k_n = 2\pi/\lambda_n = \omega/c_n$, the longitudinal sound celerity c_n , and the density of the materials ρ_n . The acoustic velocity and pressure in each layer (n) can be expressed as follows:

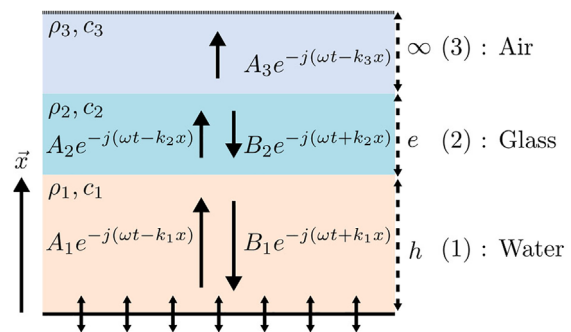


FIG. 1. (Color online) Sketch of the three layers model (not to scale). The transducer is modeled by a vibrating surface directly in contact with the water medium. A glass slide, inserted between the cavity water and the air semi-infinite medium, reflects the acoustic wave. Two interfaces are considered: the water/glass and the glass/air interfaces.

$$\begin{cases} v_n(x, t) = A_n e^{-j(\omega t - k_n x)} + B_n e^{-j(\omega t + k_n x)}, \\ p_n(x, t) = \rho_n c_n (A_n e^{-j(\omega t - k_n x)} - B_n e^{-j(\omega t + k_n x)}) \end{cases} \quad (1)$$

with A_n the velocity amplitude of the progressive propagating wave and B_n the velocity amplitude of the regressive propagating wave in the layer (n) ($n = 1, 2$, or 3).

The acoustic source vibrates with the following velocity:

$$v(t) = v_{source} e^{-j\omega t}, \quad (2)$$

v_{source} being the velocity amplitude of the transducer. It can be linked to the displacement amplitude δ by $v_{source} = \omega \delta$.

The regressive wave appears from the acoustic impedance mismatch between two media. To determine the acoustic velocity and pressure in the layer (n), the boundary conditions are used. At each interface, we assume continuity for the normal acoustic velocity and the pressure,

$$\begin{cases} v_1(0, t) = v_{source} e^{-j\omega t}, \\ v_1(h, t) = v_2(h, t), \\ p_1(h, t) = p_2(h, t), \\ v_2(h + e, t) = v_3(h + e, t), \\ p_2(h + e, t) = p_3(h + e, t). \end{cases} \quad (3)$$

Using the definitions of v_n and p_n [Eq. (1)] in the set of boundary conditions defined in Eq. (3) leads to a set of equations for the coefficients A_n and B_n . The equations system can then be solved with the matrix formulation given by Folds and Loggins (1977),

$$\begin{bmatrix} A_1 \\ B_1 \\ A_2 \\ B_2 \\ A_3 \end{bmatrix} = M^{-1} \begin{bmatrix} v_{source} \\ 0 \\ 0 \\ 0 \\ 0 \end{bmatrix}. \quad (4)$$

The coefficients of the matrix M are the following:

$$M = \begin{bmatrix} 1 & 1 & 0 & 0 & 0 \\ e^{+jk_1 h} & e^{-jk_1 h} & -e^{+jk_2 h} & -e^{-jk_2 h} & 0 \\ \rho_1 c_1 e^{+jk_1 h} & -\rho_1 c_1 e^{-jk_1 h} & -\rho_2 c_2 e^{+jk_2 h} & \rho_2 c_2 e^{-jk_2 h} & 0 \\ 0 & 0 & e^{+jk_2(h+e)} & e^{-jk_2(h+e)} & -e^{+jk_3(h+e)} \\ 0 & 0 & \rho_2 c_2 e^{+jk_2(h+e)} & -\rho_2 c_2 e^{-jk_2(h+e)} & -\rho_3 c_3 e^{+jk_3(h+e)} \end{bmatrix}. \quad (5)$$

The coefficients can be calculated with the settings of the experimental setup. For an invertible matrix M , the acoustic velocity and pressure can be estimated.

B. Acoustic energy density

For a 1D model considering plane waves, the acoustic energy density w can be expressed as the sum of the acoustic potential energy density e_k and the acoustic kinetic energy e_p ,

$$\begin{aligned} w(x, t) &= e_k(x, t) + e_p(x, t) \\ &= \frac{1}{2} \rho_n v_n(x, t)^2 + \frac{1}{2 \rho_n c_n^2} p_n(x, t)^2. \end{aligned} \quad (6)$$

This energy density w describes the energy stored by the fluid molecules, per volume unit, and is a function of time t and space x . Its unit is J/m^3 . Usually, a global acoustic energy density, averaged in time and in space, is used to estimate the acoustic energy inside the cavity,

$$E_{ac} = \frac{1}{h} \int_0^h \frac{1}{T} \int_0^T w(x, t) dt dx \quad (7)$$

with h the height of the cavity, $T = 1/f$ the period of the wave.

C. The acoustic radiation forces (ARFs) on small particles

The creation of an acoustic standing wave inside a resonant cavity leads to interactions with the particles suspended in the inviscid fluid. The scattering of the acoustic wave on a particle results in the creation of the ARF which depends on the magnitude and frequency of the acoustic wave and on the particle properties. Bruus (2012b) and Settles and Bruus (2012) studied and explained perfectly well the origins of this force. The ARF results from the time-averaged force exerted on a particle due to the scattering of the acoustic waves from the particles (Karlsen and Bruus, 2015). This force was first studied by King (1934) for incompressible spheres, then Hasegawa and Yosioka (1969) took into account the compressibility of the particles. Finally, the ARF on particles was generalized by Gorkov (1962). The domain of validity is limited to particles with a diameter d_p much smaller than the acoustic wavelength λ_{ac} (Rayleigh hypothesis). In this work, we used $15 \mu\text{m}$ particles, so the theory is valid for frequencies smaller than $f_c < c/\lambda_c$

$= c/10d_p \approx 10$ MHz. In the general case, the ARF can be expressed (Bruus, 2012b) as

$$F^{rad} = \frac{4\pi}{3} r_p^3 \frac{\partial}{\partial x} \left\{ \frac{1}{2} \left(\frac{1}{\rho_w c_w^2} - \frac{1}{\rho_p c_p^2} \right) \langle p^2 \rangle - \frac{3}{2} \frac{\rho_p - \rho_w}{2\rho_p + \rho_w} \rho_w \langle v^2 \rangle \right\} \quad (8)$$

with r_p the particle radius, ρ_w the water density, c_w the ultrasound longitudinal velocity in water, ρ_p the particle density, c_p the ultrasound velocity in the particle, $\langle p \rangle$ the time-averaged acoustic pressure, and $\langle v \rangle$ the time-averaged acoustic velocity.

D. Theoretical part: The standing wave resonator 1D model

The reflection of the wave from the water-glass interface generates a standing wave in the cavity. The resulting acoustic field can be decomposed as the superposition of a standing wave and a propagative wave. The contribution of the propagative wave is due to the transmission through glass and air media. Considering the two contributions, the acoustic velocity and pressure can be written as

$$\begin{cases} \vec{v}(x, t) = \{ a_1 \cos(\omega t - kx + \phi_1) \\ \quad + a_2 \cos(kx + \phi_2) \cos(\omega t) \} \vec{x}, \\ p(x, t) = \rho c \{ a_1 \cos(\omega t - kx + \phi_1) \\ \quad + a_2 \sin(kx + \phi_2) \sin(\omega t) \} \end{cases} \quad (9)$$

with a_1 the contribution of the propagative part and a_2 the standing wave one. These factors are linked to A_1 and B_1 given by Eq. (4) by

$$\begin{cases} a_1 = |A_1 - B_1^*|, \\ a_2 = 2|B_1|. \end{cases} \quad (10)$$

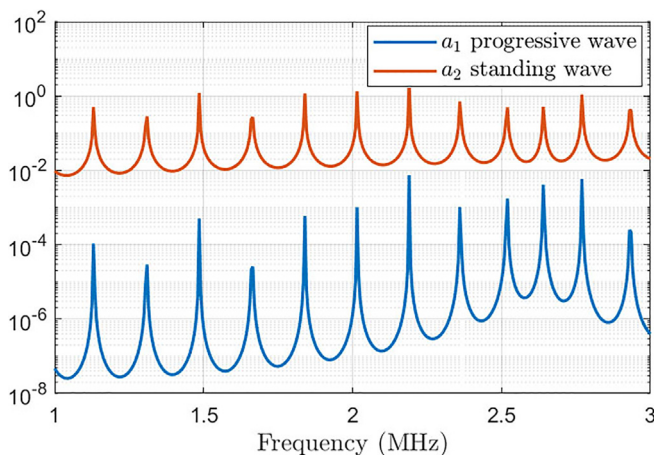


FIG. 2. (Color online) Comparison of the contributions of the progressive wave part a_1 and the standing wave part a_2 . These results are obtained by implementing Eq. (4) with the parameters $h = 4.2$ mm, $c_1 = 1500$ m s⁻¹, $\rho_1 = 1000$ kg m⁻³, $c_2 = 5500$ m s⁻¹, $\rho_2 = 2500$ kg m⁻³, $c_3 = 343$ m s⁻¹, $\rho_3 = 1.2$ kg m⁻³.

The numerical resolution of the Eq. (4) using the values of the experimental settings allow the determination of the ratio between the standing wave (a_2) and the progressive wave (a_1) contributions on the Fig. 2.

From this result, we can consider that the ARF acting on the particles is mainly due to the standing wave. By neglecting the propagative part, the standing acoustic velocity and pressure can be written as

$$\begin{cases} \vec{v}(x, t) = v_m \cos(kx + \phi) \cos(\omega t) \vec{x}, \\ p(x, t) = \rho_w c_w v_m \sin(kx + \phi) \sin(\omega t) \end{cases} \quad (11)$$

with v_m the magnitude and ϕ the phase, depending on the boundary limits.

From the previous hypothesis and Eqs. (6), (7) we deduce E_{ac} for a purely standing wave,

$$\begin{aligned} E_{ac} &= \frac{1}{L} \int_0^L \frac{1}{4} \rho_0 (v_m)^2 \{ \sin^2(k(x-L)) \\ &\quad + \cos^2(k(x-L)) \} dx \\ &= \frac{1}{4} \rho_0 (v_m)^2. \end{aligned} \quad (12)$$

From Eq. (8), we calculate the ARF,

$$F^{rad} = 4\pi r_p^3 \beta k E_{ac} \sin(2kx + 2\phi). \quad (13)$$

β is the acoustic contrast factor given by

$$\beta = \frac{\rho_p + \frac{2}{3}(\rho_p - \rho_w)}{2\rho_p + \rho_w} - \frac{\rho_w c_w^2}{3\rho_p c_p^2} = \beta_d + \beta_c. \quad (14)$$

The acoustic contrast factor is decomposed as the sum of the density ratio β_d and the compressibility ratio β_c . If $\beta > 0$ (respectively, $\beta < 0$), the particles will move toward the pressure node (respectively, antinode). This ARF generated by a standing wave is illustrated in Fig. 3.

The theoretical 1D model is then evaluated using Eqs. (12) and (13) with the numerical values corresponding to the experimental conditions. v_m is deduced from Eqs. (10) and (4). The following geometric and physical parameters for the three layers are implemented in the model: $h = 4.2$ mm, $c_1 = 1500$ m s⁻¹, $\rho_1 = 1000$ kg m⁻³, $c_2 = 5500$ m s⁻¹, $\rho_2 = 2500$ kg m⁻³, $c_3 = 343$ m s⁻¹, $\rho_3 = 1.2$ kg m⁻³. The boundary condition for the transducer velocity is defined as $v_{source} = \omega \delta$ with $\delta = 1.10 \cdot 10^{-9}$ m [typical value used by Bruus (2012a)].

Using Eqs. (4) and (12) it is then possible to compute the variation of the acoustic energy inside the cavity as a function of the acoustic frequency from 1 to 3 MHz. The result is shown in Fig. 4. One can see the successive peaks of acoustic energy corresponding to the resonance conditions for a multi-node configuration. As we are dealing with a simple model with perfect boundary conditions and no dissipation losses except from the air layer, the peaks are narrow with a large difference with the minima of acoustic energy, corresponding to a high quality factor Q .

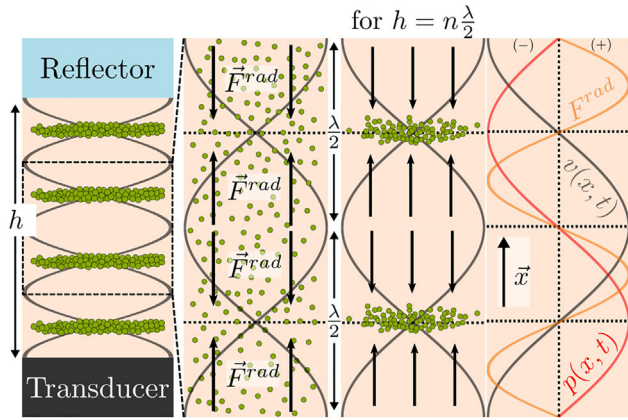


FIG. 3. (Color online) Sketch of the multi-node cavity in a perfect resonance configuration. If we consider a purely reflector, the cavity height must match an integer of the half acoustic wavelength to maximize the acoustic energy (figure on the left). The three figures on the right side are a zoom around the two central pressure nodes shown on the left. The ARF, generated by the purely or partially standing wave, pushes the particles (if $\beta > 0$) toward the pressure node. The ARF, at the resonance condition ($h = n(\lambda/2)$), is modulated with a spatial period two times smaller than the acoustic pressure and velocity. The pressure and the velocity are in a phase quadrature.

We also can compute the axial positions of the acoustic pressure nodes by implementing the acoustic pressure and velocity from Eq. (4), and then the acoustic radiation force from Eq. (13). It is possible to compute the evolution of the amplitude of the ARF as a function of the axial position for an acoustic frequency varying from 1 to 3 MHz. The result is shown in Fig. 5 as a contour plot of the amplitude of the ARF as a function of x and F_{ac} . The red curves correspond to the levitation planes. One can see clearly the number of acoustic nodes (i.e., levitation planes) increasing for increasing acoustic frequency. The important point is that the evolution is continuous: the number of nodes increases continuously while the acoustic levitation planes are moved toward the lower wall. It means that the levitation planes do not vanish away from the resonance. They even can be moved along the height of the cavity just by changing the acoustic frequency, even far from the resonance.

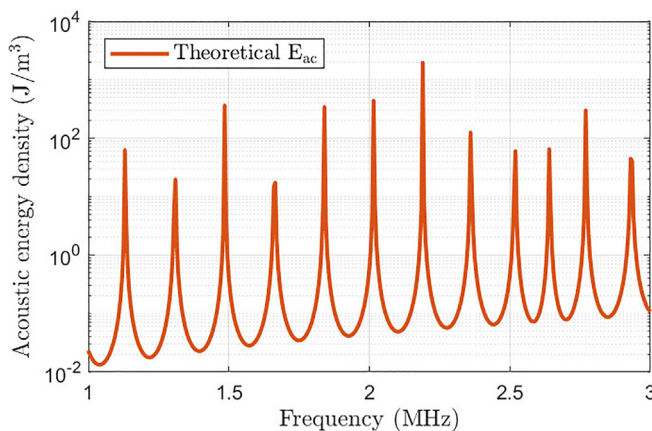


FIG. 4. (Color online) The acoustic energy density E_{ac} is computed with the 1D model using Eqs. (4) and (12).

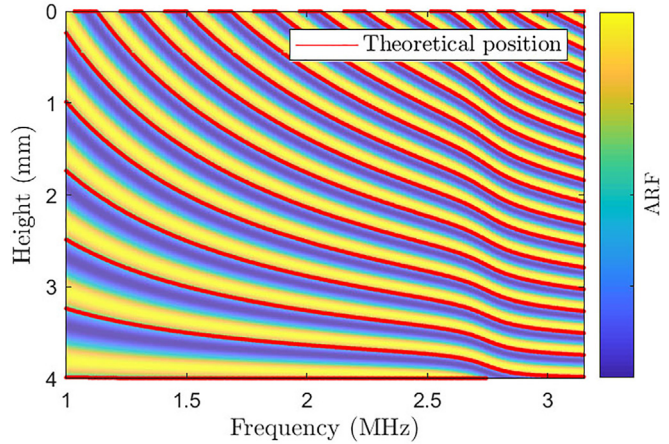


FIG. 5. (Color online) Theoretical axial positions of the nodes for increasing acoustic frequency. The contour plot shows the amplitude of the ARF, normalized for each frequency, as a function of the frequency. The red curves correspond to the position of the levitation planes.

The evolution of the node position and the discontinuities can be explained by the coupling of two resonant layers, the water and the glass ones.

E. Experimental part: Link between the ARF and the particle track

To compare with the theoretical results, we need an experimental techniques to measure the acoustic energy and the axial position of the acoustic pressure node inside a cavity. We show in this section that the motions of the particles is directly linked to the acoustic force.

Indeed, according to the Newton's second law, we can write for every particle,

$$m\vec{a} = \sum \vec{F} = \vec{F}^{buo} + \vec{F}^{rad} + \vec{F}^{sto}, \quad (15)$$

where \vec{F}^{buo} is the buoyancy force, \vec{F}^{rad} is the acoustic radiation force, and \vec{F}^{sto} is the viscous Stokes drag force applied to a particle (with a positive acoustic contrast factor) inside the cavity and moving toward an acoustic pressure node.

For 15 μm polystyrene beads, the buoyancy force is

$$F^{buo} = \frac{4\pi}{3} r_p^3 (\rho_f - \rho_p) g \approx 7 \times 10^{-12} \text{ N} \quad (16)$$

and can then be neglected. If the motion of the particle is slow and if the particle is small, the inertial effects can safely also be neglected (Augustsson *et al.*, 2011; Barnkob *et al.*, 2010; Bruus, 2012b).

Equation (15) simplifies as the simple balance between the ARF \vec{F}^{rad} and the Stokes force \vec{F}^{sto} . Using Eq. (13) and the standard expression for the Stokes force applied on a sphere \vec{F}^{sto} , we obtain

$$4\pi r_p^3 \beta k E_{ac} \sin(2kx + 2\phi) = 6\pi \eta r_p v_p \quad (17)$$

with r_p the particle radius, β the acoustic contrast factor, k the acoustic wave number, E_{ac} the acoustic energy density, η the dynamic viscosity, and v_p the particle velocity. It leads

to the following expression for the velocity of the particle moving toward the acoustic pressure node:

$$v_p(x) = \frac{2\beta r_p^2 k E_{ac}}{3\eta} \sin(2kx + 2\phi). \quad (18)$$

Using this relation, it is then possible to measure the acoustic energy simply by measuring the magnitude of the velocity of a particle whose diameter and physical properties are known using the following relation:

$$E_{ac} = \frac{3\eta}{2\beta r_p^2 k} |v_p(x)|. \quad (19)$$

Measuring the velocity magnitude gives then an easy access to the mean acoustic energy. In Sec. III we describe the experimental setup and methodology used to measure the velocity of the particles and then the acoustic energy of the system.

III. MATERIALS AND METHODS

A. Experimental setup

The setup has been designed to be fully automated, in order to carry out easily a large parametric study, i.e., to measure the evolution of the acoustic energy over a wide range of acoustic frequency with a small frequency step. Every device used in the experimental setup are controlled by a computer and can work in closed-loop (Fig. 6) a MATLAB code. First, a syringe pump (Harvard Apparatus™)

is actuated to mix the particles, and supply a homogeneous suspension of particles by alternatively pushing and pulling the medium. Once the fluid has settled, the ultrasound transducer (SignalProcessing™) and the USB digital microscope are simultaneously triggered. The motions of the particles toward the pressure nodes are then recorded until they reach the levitation plane. Then the recording is stopped and the acoustic parameters are changed before running the same protocol again.

The possibility to control each parameter of the setup allows the measurement of the acoustic energy over a wide frequency range (from 1 to 3 MHz) with a small frequency step ($\Delta F_{ac} = 0.005$ MHz) in order to find the maxima with a good resolution. Such a small frequency step over such a wide range of frequencies leads to a large amount of data recorded (2400 measurements points).

The ultrasonic transducer is powered by an arbitrary waveform generator (Handyscope HS5 from Tiepie Engineering™). A USB digital microscope (Edge from Dinolite company™) captures sequences of images with a frame-rate of 45 fps. The flow rates used to mix the particles in a suspension are 5mL/min. We used polystyrene particles (Phosphorex™) with a diameter of 15 μm .

B. Acoustofluidic chip

The chip is made of a PDMS (Polydimethylsiloxane, RTV 615, Neyco™) body bonded on a microscope cover-glass and a single element ultrasonic transducer.

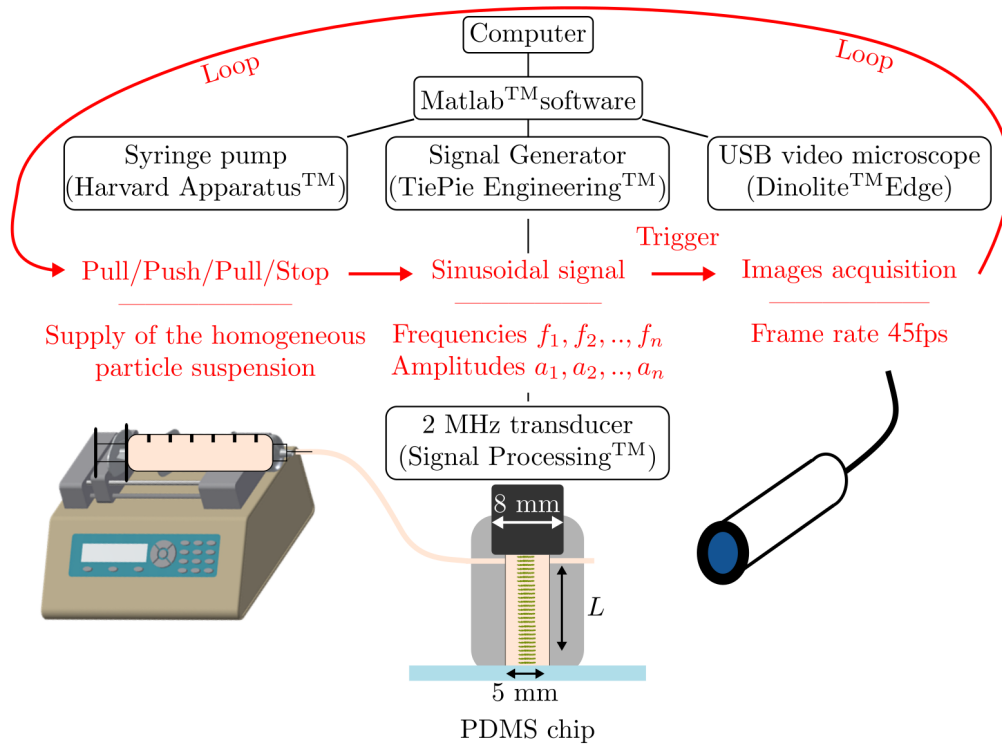


FIG. 6. (Color online) Schematic of the experimental setup. A laptop with MATLAB™ software controls the whole chain. The first step consists in homogenizing the particle suspension in the cavity through successive push-pulls of the syringe pump. Then the acoustic parameters are set before turning-on the ultrasound transducer simultaneously with the images sequence acquisition. The same sequence is repeated in a closed-loop to allow a large parametric study. In this case, the evolution of the acoustic energy as a function of the acoustic frequency can be studied over a wide frequency range.

We designed a PDMS chip for the acoustofluidic cavity. On the upper part of the cavity there is the ultrasound emitter, in contact with the fluid, avoiding acoustic losses through various interfaces. On the lower part of the cavity, we use a microscope cover-glass which acts as a powerful acoustic reflector while allowing a good optical access. The overall acoustic resonant cavity is then simple and efficient.

To shape the PDMS body, we use a negative mold made with a 3D printer (3D Form 2 from Formlabs Inc.TM). The PDMS is poured inside the mold and put in an oven at 70 °C for 24 h.

The overall dimensions of the resonant cavity are its diameter $d = 5$ mm and its height h . In the following, we will use a multi-nodes cavity, i.e., $h = N(\lambda/2)$, with $N > 1$.

C. Transducer characterization

The necessary condition to make a broadband multi-node chip relies on the use of a large bandwidth ultrasonic transducer. To explain the next results, we experimentally characterized the transducer by using self-reciprocity methods (Widener, 1980; Zhang *et al.*, 2016). The principle of these approaches uses the double reciprocity of the transducer which can both emit or receive signal (Hill and Egle, 1980). We assume that the transfer function $h(t)$ of the transducer is the same for the emission and the reception. At first approximation, we neglected the wave diffraction. By emitting a pulse signal on a reflective wall, we can measure the frequency response $H_{transducer}(f)$ of the transducer with the received signal. The electrical received signal $r(t)$ is expressed as

$$r(t) = e(t) * h(t) * h(t) \tag{20}$$

with $e(t)$ the electrical emitted signal, $*$ the convolution product, and $h(t)$ the impulse response of the transducer.

Passing in the Fourier transform domain, we finally find the frequency response of the transducer $H_{transducer}(f)$,

$$H_{transducer}(f) = \sqrt{\frac{R(f)}{E(f)}} \tag{21}$$

with $E(f)$ the Fourier transform of the emitted signal $e(t)$ and $R(f)$ the Fourier transform of the received signal $r(t)$.

To cover the interesting bandwidth, one sinusoidal period with the carrier frequency of 2 MHz was emitted. The result is shown on Fig. 7. One can see that the transducer indeed works over a wide frequency range, with a maximum at its optimal frequency.

D. PIV method

In order to measure the particle velocity, a particle image velocimetry (PIV) method is used. PIV is a measurement technique used to measure velocity fields through the displacements of particles between two successive snapshots.

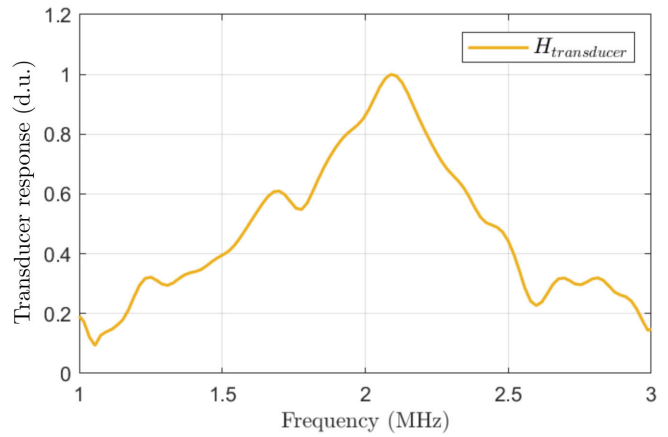


FIG. 7. (Color online) Estimation of the transducer frequency response $H_{transducer}(f)$ with the self-reciprocity method.

The principle consists in computing the cross correlation between two successive snapshots which are divided into interrogation windows (IW). The cross-correlations are computed over each IW, leading to one velocity vector per IW. To manage our data, we have used the PIVlab software on MATLABTM, developed by Thielicke (2014) and Thielicke and Stamhuis (2014).

From the movies of the transient focusing [Fig. 8(a)] of particles toward the acoustic nodes, we extract the map of velocities [Fig. 8(b)] using PIVlab. We used an IW size of 64 pixels for the first pass. The second pass used a 32 pixel IW. In both cases we used a 50% overlap to increase the spatial resolution. No intensity threshold or pre-processing was applied to the raw images.

E. Parametric study of the axial velocity

The PIV measurements gives us access to the axial acoustic focusing velocity profile along the vertical axis of the acoustic chamber, which means the focusing velocity towards multiple pressure nodes. With the determination of the particle velocity maxima along the x axis, we can deduce the ARF x -profile and then the acoustic energy as a function of the frequency.

The main steps are summarized on Fig. 8. First, from the eight-bit gray-scale images [Fig.8(a)], the instantaneous PIV fields are calculated [Fig. 8(b)]. Before the triggering of the acoustic emission, the axial velocity is almost null [Fig. 8(b), first field on the left]. The velocity is not null because the particles are still in motion after their injection into the cavity. Once the ultrasounds are turned-on, the PIV fields show quickly the expected sinusoidal pattern along the axial direction [Fig. 8(b), $t = 50$ ms]. The whole velocity field is spatially averaged along the radial direction to obtain axial profiles of axial velocity [Fig. 8(c)]. Then, the first eight velocity profiles following the acoustic trigger are selected and averaged in time (step 3). Finally, we estimate the velocity maximum by calculating the root mean square value (RMS) weighted by $\sqrt{2}$ over the time-averaged velocity profile (step 4). This process is then applied

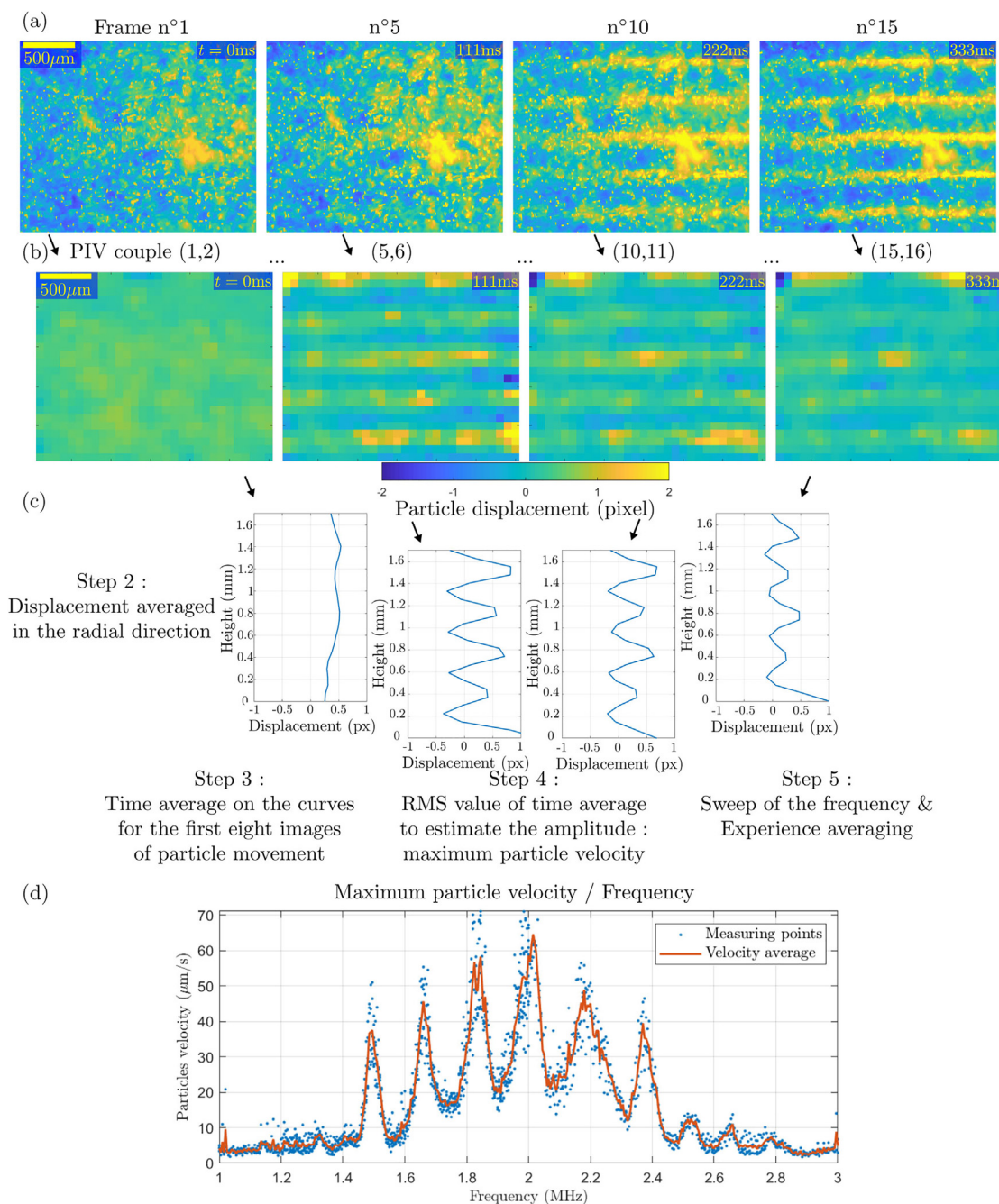


FIG. 8. (Color online) (a) Snapshots (eight-bit gray-scale) of the resonant cavity (side-view) acquired with the USB video microscope. The frame rate is 45 fps. It illustrates the acoustic focusing of the particles from $t = 0$ (no US) to 355 ms (particles focused in the levitation planes) for a given voltage applied to the transducer (7 V). (b) PIV images obtained with PIVlab from the snapshots time-series. (c) Post-processing steps of the velocity fields: the PIV fields are spatially averaged along the radial direction, leading to a vertical profile of axial focusing velocity from which the amplitude of the velocity is derived. The final step consists in varying the acoustic frequency to evaluate the evolution of the particle velocity as a function of the acoustic frequency. (d) Evolution of the particles focusing velocity as a function of the acoustic frequency. Six large peaks of axial velocity can be seen in the frequency band ranging from 1.4 to 2.4 MHz.

systematically for a parametric study of the maximum velocity as a function of the acoustic frequency over a wide frequency range ($1 \leq F_{ac} \leq 3$ MHz).

We show on Fig. 8(d) a typical example of the evolution of the maximum axial velocity of the particles as function of the acoustic frequency. As expected, one can see clear and sharp maxima corresponding to the acoustic

resonances found when changing the number of pressure nodes.

F. Estimation of the node position

Another interesting feature is to measure the axial location z_{foc} of the pressure nodes as a function of the acoustic

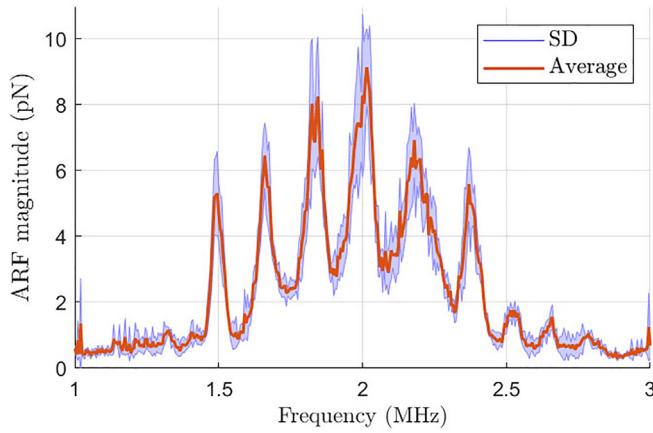


FIG. 9. (Color online) The ARF magnitude is plotted as a function of frequency for a given voltage (7 V). The average and the standard deviation of the measurement are presented.

frequency. One can expect that it will also depends on F_{ac} , as previously observed in a single node acoustic trap (Dron and Aider, 2013) and as shown with the 1D model.

In order to estimate the position of the nodes, we are no longer interested in the transient steps of acoustic focusing. We need stable acoustic levitation planes. For this reason, the first step consists in forming stable aggregates over the full height of the cavity. Then, we sweep the acoustic frequency from 1.7 to 2.5 MHz. Simultaneously the camera records the evolution of the aggregates' positions. We then select the correct region of interest, before applying a projection in the radial direction by selecting the maximum intensity of the pixels at each axial position leading to the axial locations of each aggregate.

IV. RESULTS

In the following we will consider two different heights for the cavity: $h = 4.2$ and 10 mm.

A. Evolution of the acoustic energy over a broadband spectrum for $h = 4.2$ mm

From the particles velocity, we deduce the ARF magnitude by using Eq. (17). The particle velocity and the ARF magnitude are related by the proportional coefficient ($-6\pi\eta r_p$). We observe several resonance peaks for increasing acoustic frequency (see Fig. 9). Each peak corresponds to the creation of a new node in the acoustic cavity. One can also see that the velocity is maximum for $f_{ac} = 2$ MHz, which corresponds to the optimal resonant frequency of the acoustic transducer. The measurement is highly reproducible with a small average standard deviation on all the frequencies ($\overline{SD} = 3.35 \pm 3.15 \mu\text{m/s}$).

The prior knowledge of the particle properties allows to estimate the acoustic energy density (E_{ac}) (Fig. 10) with the Eq. (19). For the frequencies ranging from 1.5 to 2.75 MHz, one can see multiple maxima with the maximum values of the acoustic energy density reaching 1.5 J/m^3 . Nevertheless, at the anti-resonance the acoustic focusing is still working

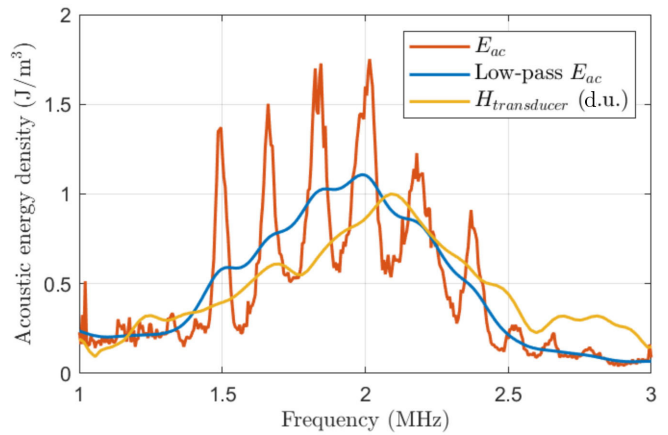


FIG. 10. (Color online) Estimation of the acoustic energy density as a function of the frequency. The acoustic energy density (red curve) has been calculated from the particle velocity [Fig. 9 and by using Eq. (19)]. To highlight the broadband of the system, the acoustic energy density signal has been low-pass filtered (blue curve) and compared to the frequency response of the transducer (yellow curve in an arbitrary unit).

with an energy density about 0.5 J/m^3 , only three times lower than the maximum found at the resonance. The resonance peaks of the cavity are narrow and the resonance frequencies can clearly be identified.

The comparison, on the Fig. 11, between the acoustic energy density given by the experiments and the theoretical 1D model (see Sec. IID for more details) shows a very good agreement for the resonance peaks positions. However, we denote a mismatch with the shapes of the curves. This difference can be explained by several reasons as the characteristic of the acoustic source and the quality factor Q of the experimental cavity. We used a packaged wideband ultrasonic transducer which has its own energy distribution as a function of the acoustic frequency (see yellow curve on the Fig. 10). The maximum is obtained at the resonant frequency of this 2 MHz transducer nearby the maximum of the frequency response of the transducer obtained with the self-reciprocity method (see Sec. III C). Outside of the emission limits, about 1.5 and 2.5 MHz, the transducer converts

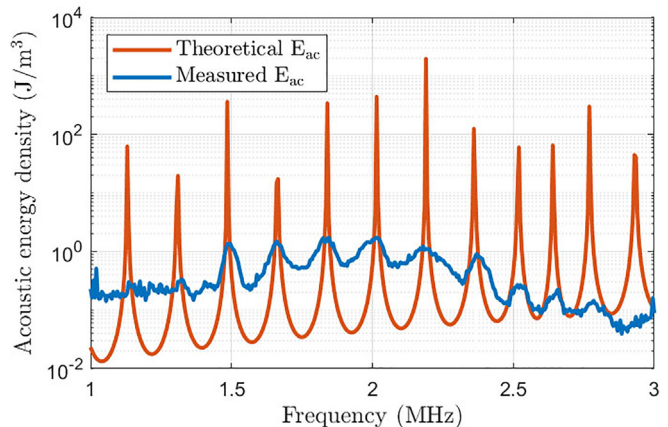


FIG. 11. (Color online) Comparison of the acoustic energy density E_{ac} estimated through experimentation (for a 7 V voltage) with the theoretical 1D model.

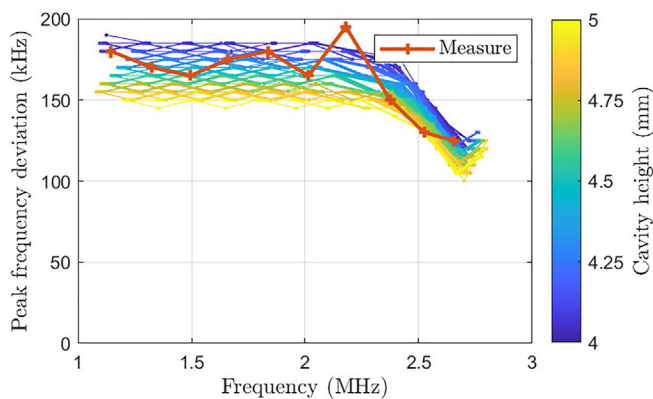


FIG. 12. (Color online) Comparison of the frequency gaps calculated with the theoretical model for different heights and the ones given by the PIV experiment by the PIV experiment for a cavity height about $h = 4.2$ mm.

little energy in acoustic waves, and the resonance phenomenon is lower. A better theoretical model would have taken the transducer frequency response in the calculation of the acoustic energy density. The second explanations can be found in the difference in the Q factor. The 1D theoretical model does not consider the energy losses by the cavity boundaries from the transducer diffraction neither the parallelism between the transducer and the reflector. The acoustic streaming (Wiklund *et al.*, 2012) is also not taken into account and would have decreased the Q factor.

The actual height of the cavity can also be checked by comparing the frequency gap between two maxima found with the model and the ones calculated from the experiment. In Fig. 12 we vary the input height in the model. By minimizing the mean error we determine the height. In this case, the cavity height is estimated at $h = 4.2$ mm.

B. Estimation of the acoustic energy on a broadband spectrum for $h = 10$ mm

We applied the same process to a larger cavity ($h = 10$ mm). The acoustic energy density is shown in

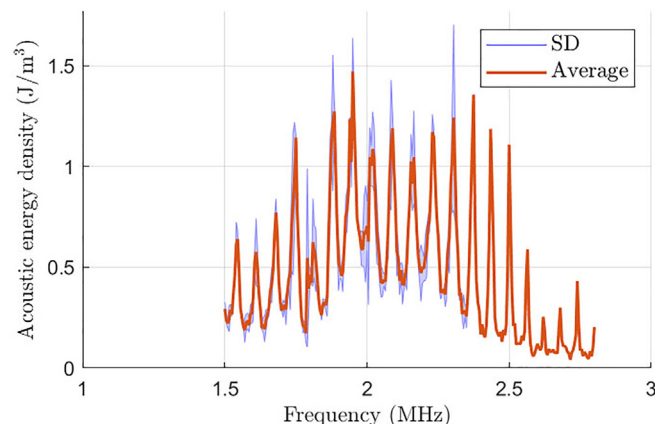


FIG. 13. (Color online) Estimation of the acoustic energy density for a cavity height about $h = 10$ mm. The acoustic energy density has been calculated from the particle velocity [Fig. 9 and by using Eq. (19)].

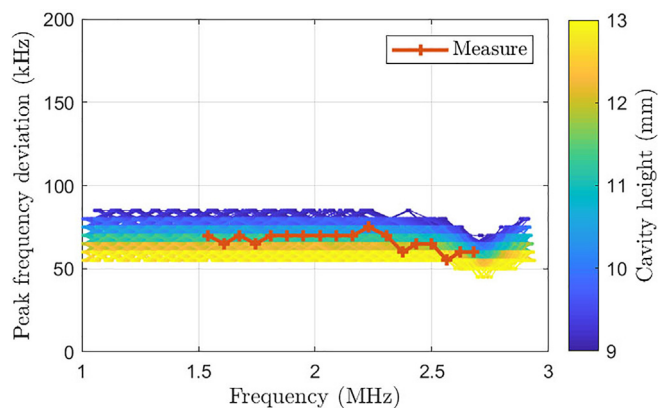


FIG. 14. (Color online) Comparison of the frequency gaps calculated with the theoretical model for different heights and the ones given by the PIV experiment by the PIV experiment for a cavity height about $h = 10$ mm.

Fig. 13. As for the 4 mm cavity, the distribution of the energy spreads from 1.5 to 2.75 MHz. The minima of E_{ac} are the same as in Fig. 10. The main difference is the frequency band between the resonance peaks. As expected by the theory, the number of resonance peaks increases with the height of the cavity, for the same frequency band.

The frequency gaps can also be compared to the theoretical model. By fitting the measured peak to the theoretical 1D model (Fig. 14), we estimate the height to $h = 11.0$ mm.

C. Evolution of the axial node positions as a function of the frequency

Another interesting feature of the setup is that the axial positions of the aggregate can be varied continuously using the acoustic frequency as a control parameter. Indeed, the Fig. 10 shows that the acoustic energy remains significant between the resonance peaks, instead of vanishing as one could expect. The consequence is that the levitation planes can be moved smoothly nearly over the entire height of the cavity, from one resonance frequency to the other, just by tuning the acoustic frequency. This is illustrated in Fig. 15, where the axial positions of the aggregates measured experimentally perfectly fit the positions found by the theoretical 1D model. The relation between the node positions and the frequency is not linear and depends on the axial position of the aggregate. In this experiment we find an amplitude for the axial displacement about $920 \mu\text{m}$ for the upper node and about $170 \mu\text{m}$ for the lower node, for a frequency ranging from 1.7 to 2.5 MHz.

V. MANIPULATION OF CELL SPHEROIDS

In this section, we address with our approach a major issue in the modern cell-biology (Cai *et al.*, 2021; Miura *et al.*, 2020): the formation, culture, and manipulation of cell spheroids inside a cell-culture chip.

A. MSC isolation and characterization

MSCs were isolated from adipose tissue of the thigh of a healthy donor, after a signed consent, according to the

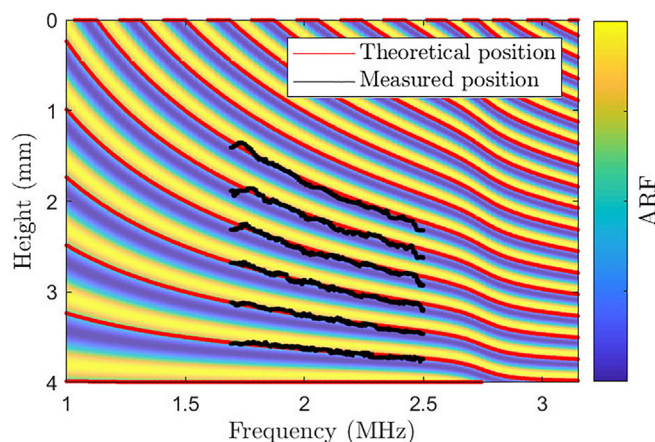


FIG. 15. (Color online) Comparison between the theoretical and experimental axial positions of the nodes for increasing acoustic frequency. The black lines correspond to the experimental measurements. The contour plot shows the amplitude of the ARF, normalized for each frequency, as a function of the frequency and the axial position.

French regulations. MSCs were obtained after the digestion of adipose tissue with collagenase NB6 (SERVA ELECTROPHORESIS, Heidelberg, Germany). The adipose tissue was placed in 40 ml of collagenase NB6 diluted in α -MEM medium at a final concentration of $5\mu\text{g}/\text{ml}$ in a 50 ml conical tube (Falcon, Dutscher, Bernolsheim, France). After a 2 h incubation at 37°C , the digested tissue was filtered through a cell strain with pores of $100\mu\text{m}$ to remove the remaining tissues. The strained cells were then centrifuged and plated in a cell factory (Thermofisher, Nunc, Waltham, United States) for expanding in MSC culture medium composed of α -MEM (Gibco, Thermofisher, Waltham, United States) supplemented with 10% fetal bovine serum (FBS, Biowest, Nuaillé, France) and 1% antibiotic/antimycotic

mix (Anti-Anti 100 \times , Gibco, Thermofisher, Waltham, United States).

B. Formation of spheroids of MSCs in acoustic levitation

The protocol used by Jeger-Madiot *et al.* (2021) was applied to form spheroids with hMSCs, of sizes about $20\mu\text{m}$, in acoustic levitation. After about ten hours of culture in acoustic levitation, the monolayers of hMSCs, located at each pressure node, spontaneously self-organized into spheroids of a typical diameter close to $400\mu\text{m}$. A typical time-lapse is shown in Fig. 16.

It is important to emphasize that once the spheroids are formed, they can be maintained and cultured as long as needed (several days) in acoustic levitation (Jeger-Madiot *et al.*, 2021). This result may be surprising as the spheroids are large ($d_{\text{spheroid}} \approx \lambda_{\text{ac}}$) and no longer respect the Rayleigh approximation ($d_p \ll \lambda_{\text{ac}}$). The theoretical expression used for the ARF [Eq. (13) is probably no longer valid and a new theoretical background should be derived (Baasch and Dual, 2018)], but this point is beyond the scope of the current study. Micro-gravity experiments (Dumy *et al.*, 2020) are currently carried out to try to study the acoustic levitation of large objects.

Once the spheroids are formed, different manipulations can be applied. In particular, following the theoretical results obtained with 1D model, the axial positions and the axial spacings between the spheroids can be controlled just by varying the acoustic frequency.

C. Estimation of the spheroids axial positions

In order to characterize the evolution of the positions of the spheroids with the frequency shift, we used a home-made MATLAB image analysis code. It works automatically

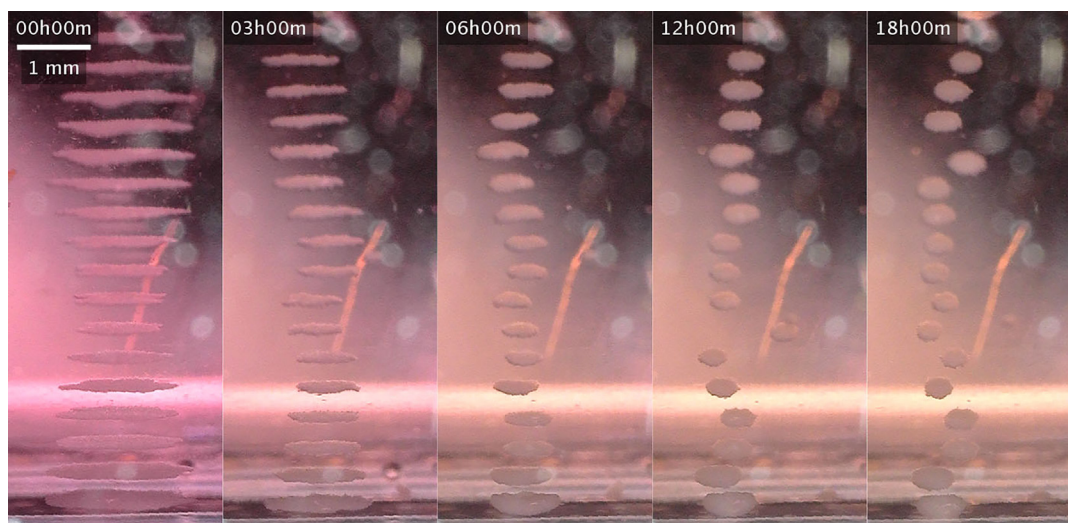


FIG. 16. (Color online) Time-lapse of snapshots of the culture of hMSC cells in acoustic levitation. The snapshots are taken from the side of the cavity ($h = 10\text{mm}$). At the beginning, the cells are trapped in thin layers at each acoustic nodes. Then during the first hours, the cells sheets spontaneously self-organize into stable spheroids with a typical diameter close to $400\mu\text{m}$ (Jeger-Madiot *et al.*, 2021). The whole time lapse is available in the supplementary video 3.¹

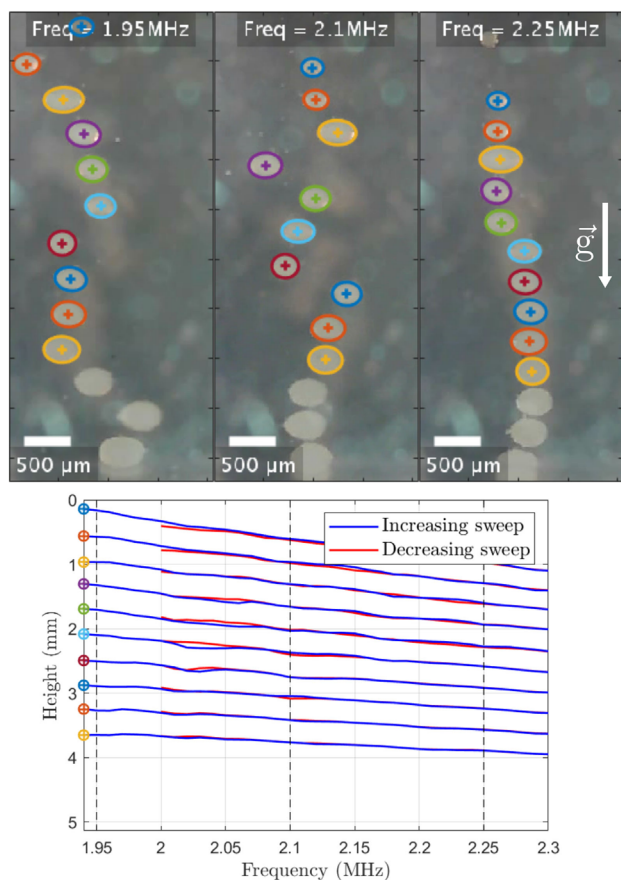


FIG. 17. (Color online) (a) Visualization of the spheroids of MSCs in acoustic levitation. Each spheroid is identified and can then be tracked. The variation of their positions for three different acoustic frequencies can be seen clearly on the three snapshots. (b) It is then possible to control the spheroids axial positions by varying the acoustic frequency. It is illustrated for an increasing frequency between 1.94 and 2.3 MHz (blue lines), then a decreasing frequency between 2.3 and 2.0 MHz (red lines). It demonstrates that this manipulation is reversible. Reducing the distance between two spheroids allows their merging as will be discussed in the following. See also the supplementary video 1.¹

with a few user-defined parameters and once the regions of interest (ROIs) for each spheroid have been manually defined. Then an ellipsoid is fitted on the binarized image. The positions of the ellipse centers provide the axial positions of the spheroids. For the whole image sequence, ROIs were defined automatically from the ellipsoid characteristics of the previous image. We obtained the evolution of the axial positions of the spheroids as a function of the acoustic frequency.

D. Control of the axial position

As previously shown with the particles, cell spheroids can be moved just by varying the acoustic frequency. This manipulation is shown on the Fig. 17 where the acoustic frequency varies from 1.94 to 2.3 MHz. The upper spheroid moves from an axial position about $z = 0.14$ to 1.10 mm and the lower one from $z = 3.65$ to 3.95 mm, which correspond, respectively, to a displacement about 2.67 and 0.83 mm/MHz. The average

distance between two spheroids changes from 39 to 32 μm which corresponds to a decrease in 20 $\mu\text{m}/\text{MHz}$.

E. Control of the axial ARF: Isoforce manipulation

For a given setup, the characterization of the forces in the acoustic cavity provides the predefined pattern of the applied forces as a function of the frequency and the amplitudes of the generator signal. Using this knowledge, it becomes possible to handle the spheroids with a constant amplitude ARF.

For a given configuration, we made a parametric study to obtain the signature of the acoustic cavity as a function of the frequency and the amplitude [Fig. 18(a)]. To limit the amount of data we arbitrarily chose a limited range of frequencies [2 – 2.085 MHz] and of amplitudes [5 – 10 V]. On this frequency range, we observe two resonance peaks and one anti-resonance minimum.

The variation of ARF magnitude can be rescaled by V^2 leading to a collapse of all curves of Fig. 18(a) onto the same single curve with the same evolution with the frequency [Fig. 18(b)]. A parabolic dependence between the ARF amplitude and the acoustic frequency can be derived for various voltages applied to the transducer,

$$ARF(f_{ac}) = a(f_{ac})V^2,$$

with f_{ac} the acoustic frequency and $a(f_{ac})$ the resonance coefficient depending on f_{ac} . This result was expected as far as the acoustic pressure delivered by the transducer is directly proportional to the applied voltage.

Finally, from Fig. 18(b), the suitable voltage can be calculated to compensate the variation of the amplitude of the ARF when changing the acoustic frequency. Instead of using a constant voltage for all the frequencies, we vary the voltage to compensate the variation of ARF using the inverse of the average of the curves shown on Fig. 18(b). The voltage variation as a function of the frequency needed to have a constant acoustic force (2 pN in this case) on the whole frequency range is shown in Fig. 18(c). It shows a maxima for the anti-resonance frequency and two minima for the resonance frequencies. Using this variation of voltage, it becomes possible to move the spheroids keeping the ARF magnitude constant.

F. Assembly of two spheroids

One possible application is the merging of cells spheroids. After the first step of self-organization of the spheroids in acoustic levitation, it is possible to bring them closer and closer just by varying the acoustic frequency (and varying the voltage to keep the ARF constant). This manipulation promotes the interactions between the spheroids. In Fig. 19, the spheroids are brought closer to each other. After 16 h, the two central spheroids begin to interact and to finally merge. One hour later, an assemblid composed with two spheroids could be trapped and maintained in acoustic levitation. This result demonstrates that it is now possible to

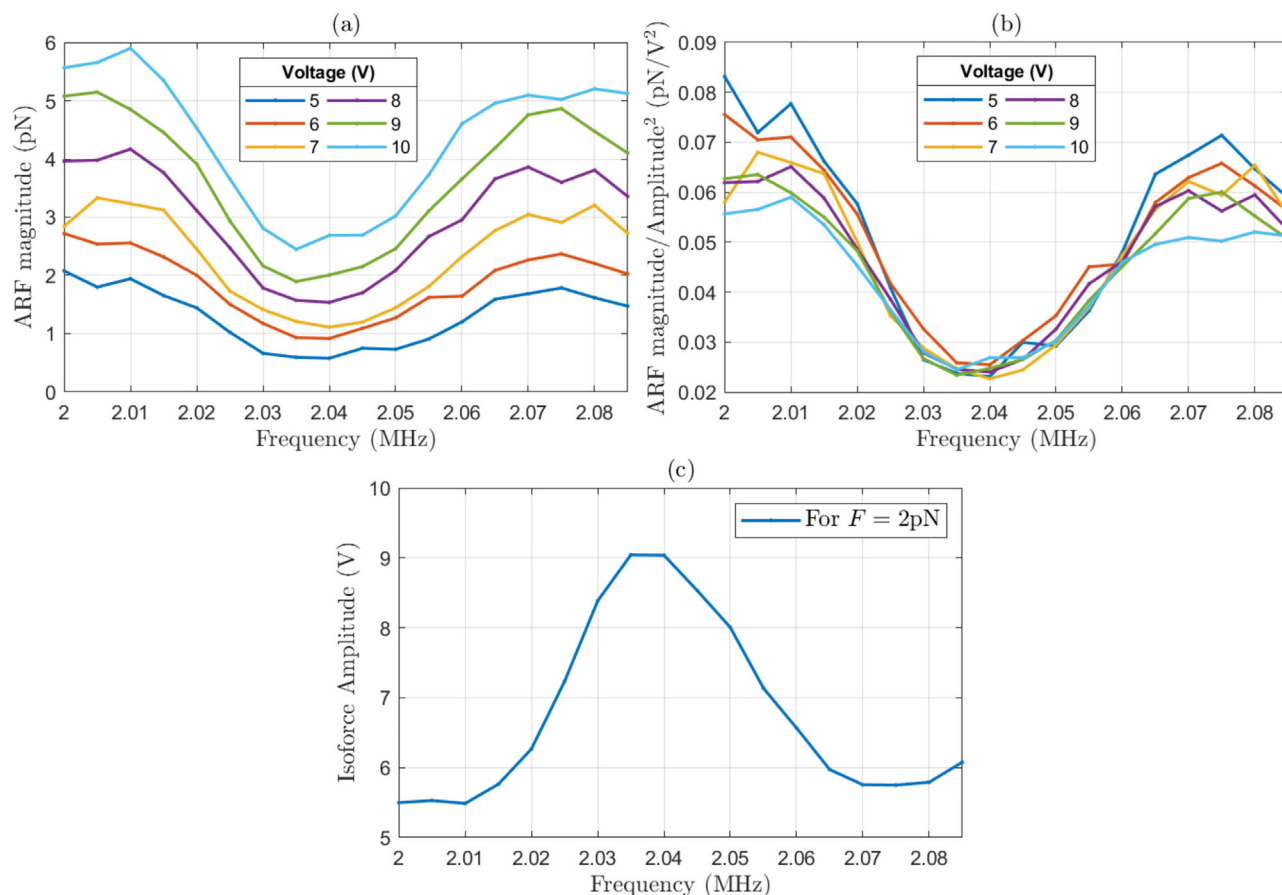


FIG. 18. (Color online) Estimation of the isoforce voltage amplitude to move spheroids with a constant ARF magnitude. (a) Measure of the magnitude ARF in the range [2 – 2.085MHz] for input voltage from 5 to 10 V. (b) Normalization by the square voltage amplitude. (c) From the average of the previous curves, we deduce the voltage amplitude needed to stabilize the applied ARF on spheroids to $F = 2\text{pN}$.

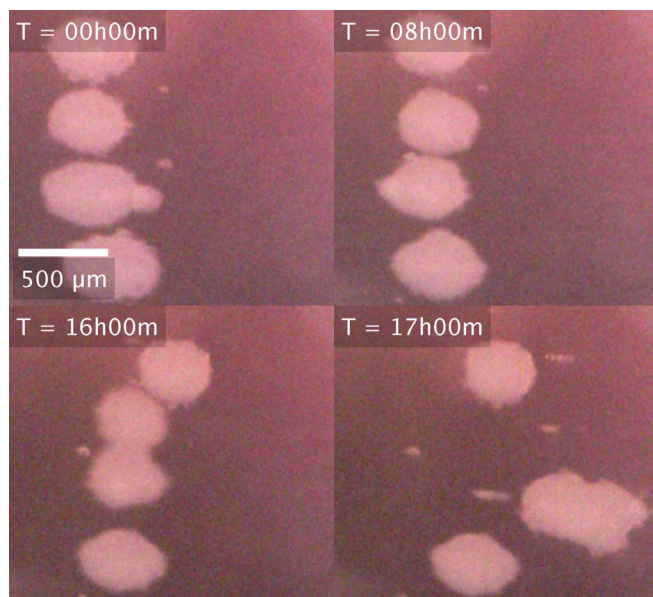


FIG. 19. (Color online) Manipulation of hMSC spheroids in acoustic levitation. At $T = 0$, the spheroids have already moved and the spacing between them has been reduced (See the supplementary video 2¹ for the time-lapse of the process). After 16 h we can see the merging of the two central spheroids. The instability of the new acoustic trap brings the assemblid to the lower node.

create, culture and assemble spheroids of cells in acoustic levitation just by tuning the acoustic parameters.

VI. CONCLUSION

We have presented an automated experimental setup for the characterization of a large frequency bandwidth of the acoustic energy density in a standing-wave cavity.

The easy implementation and the high reproducibility of this approach provides a rapid identification of the best working frequencies and an accurate estimation of the force magnitude applied on the particle from the measurement of the particle velocities.

The high aspect ratio between the size of the ultrasound emitter and the acoustic wavelength justifies the use of a one-dimensional acoustic model. The spatial distribution of the particle velocities shows an homogeneous radial symmetry [Fig. 8(b)] along the center axis of the transducer and confirms, as first approximation, the use of plane waves to describe our chip.

As expected by the theory, increasing the cavity height leads to more resonance peaks over the frequency spectrum. Furthermore, the ARF is strong enough, in the case of a light material, to continuously trap, move and maintain the cells

or the aggregates over a wide frequency bandwidth, in this study from 1.5 to 2.75 MHz.

The comparison of the frequency resonance gaps between the experimental results and the modelling allows one to estimate with accuracy the height dimension of the cavity.

In this article we have reported the design and the characterization of a broadband multi-node standing wave cavity with the ability to trap or move object in a controlled manner. This approach, integrated with other physical or biological aspects, opens the path of large acoustofluidic applications.

The knowledge of the ratio of the maximum to minimum of the acoustic energy density on the working spectrum provides a control lever to adjust the magnitude force applied to the particles. This parameter is essential to flow acoustophoretic applications, like particle focusing or separation.

The possibility to continuously shift the position of each node allows for example the spatial manipulation of the trapped aggregate but also the direction change of the focus position in a flow configuration (Kandemir *et al.*, 2021). By leaping the frequency, an aggregate of particles could be maintained in the same position with different frequencies.

The use of the 1D acoustic model will be helpful to properly design new setups. This simple model can eventually take into account more complex designs, especially a supplementary layer (a classic transmitter layer, for instance) in the chip.

The proof of concept of a straightforward application has been validated with the merging of two hMSCs spheroids. We show the possibility to handle and to move a column of spheroids, to bring them closer to finally promote their merging. For more accurate manipulation and control of the applied ARF, it is also possible to move the spheroids with a constant force, using the preliminary characterisation of the cavity signature.

This work is the first proof of concept showing that it is possible to move and merge cells spheroids in acoustic levitation which is a crucial step for cell therapy and organoids fabrication.

ACKNOWLEDGMENTS

The authors wish to acknowledge Région Ile-de-France, the DIM ELICIT and Sorbonne Université Emergence for their financial support. The authors would like to thank Briac Thierry, Lousineh Arakelian, and Jérôme Larghero for the collect and the donation of MSCs. There are no conflicts of interest to declare. We declare that all methods in the manuscript were carried out in accordance with relevant guidelines and regulations given by the Ethical Principles of the ASA. All procedures involving patients were conducted according to the Helsinki Declaration. Mesenchymal stem cells were isolated from the adipose tissue of a male donor, obtained at Necker-Enfants Malades hospital in Paris, France. The adipose tissue was the surgical leftover and was used for research purposes after a signed consent from the donor and his parents as the legal tutors, according to the French bioethical and medical research regulations. In France, according to the law “loi Jardé” (article L. 1121-1 of

the public health code) governing scientific research on human subjects and tissue samples, the surgical leftover can be used for scientific research without the prior approval of an ethical committee.

APPENDIX

By using Eq. (8), we can write

$$\begin{aligned}
 F^{rad} &= \frac{4\pi}{3} r_p^3 \left\{ a \frac{\partial \langle p^2 \rangle}{\partial x} - b \frac{\partial \langle v^2 \rangle}{\partial x} \right\} \\
 &= \frac{4\pi}{3} r_p^3 \left\{ a (\rho_w c_w)^2 + b \right\} k v_m^2 \cos(kx + \phi) \sin(kx + \phi) \\
 &= \frac{4\pi}{3} r_p^3 \left\{ a (\rho_w c_w)^2 + b \right\} k v_m^2 \frac{1}{2} \sin(2kx + 2\phi) \\
 &= \frac{4\pi}{3} r_p^3 \left\{ 1 - \frac{\rho_w c_w^2}{\rho_p c_p^2} + 3 \frac{\rho_p - \rho_w}{2\rho_p + \rho_w} \right\} \\
 &\quad \times \frac{1}{2} \rho_w k v_m^2 \frac{1}{2} \sin(2kx + 2\phi) \\
 &= \frac{4\pi}{3} r_p^3 \left\{ 1 - \frac{\rho_w c_w^2}{\rho_p c_p^2} + 3 \frac{\rho_p - \rho_w}{2\rho_p + \rho_w} \right\} k E_{ac} \sin(2kx + 2\phi) \\
 &= 4\pi r_p^3 \left\{ \frac{\rho_p + \frac{2}{3}(\rho_p - \rho_w)}{2\rho_p + \rho_w} - \frac{\rho_w c_w^2}{3\rho_p c_p^2} \right\} k E_{ac} \sin(2kx + 2\phi) \\
 &= 4\pi r_p^3 \beta k E_{ac} \sin(2kx + 2\phi) \tag{A1}
 \end{aligned}$$

with β the contrast factor.

We define the acoustic energy density as

$$E_{ac} = \frac{1}{\lambda} \int_0^\lambda \frac{1}{2} \rho_w v(x)^2 dx = \frac{1}{4} \rho_w v_m^2. \tag{A2}$$

¹See supplementary material at <https://www.scitation.org/doi/suppl/10.1121/10.0011464> for a video of the variation of the axial positions of the spheroids depending on the frequency shift (SuppPub1.avi) (the distance between spheroids decreases for increasing acoustic frequency), a video showing how spheroids are getting closer before finally merging just by varying the acoustic frequency (SuppPub2.avi), and time-lapse showing how a cell sheet of hMSC spontaneously turns into spheroids while maintained in acoustic levitation (SuppPub3.avi) [this self-organization of MSC cells was first shown in Jeger-Madiot *et al.* (2021)].

- Augustsson, P., Barnkob, R., Wereley, S. T., Bruus, H., and Laurell, T. (2011). “Automated and temperature-controlled micro-PIV measurements enabling long-term-stable microchannel acoustophoresis characterization,” *Lab Chip* **11**(24), 4152–4164.
- Augustsson, P., and Laurell, T. (2012). “Acoustofluidics 11: Affinity specific extraction and sample decomplexing using continuous flow acoustophoresis,” *Lab Chip* **12**(10), 1742–1752.
- Baasch, T., and Dual, J. (2018). “Acoustofluidic particle dynamics: Beyond the Rayleigh limit,” *J. Acoust. Soc. Am.* **143**(1), 509–519.
- Barnkob, R., Augustsson, P., Laurell, T., and Bruus, H. (2010). “Measuring the local pressure amplitude in microchannel acoustophoresis,” *Lab Chip* **10**(5), 563–570.
- Bruus, H. (2012a). “Acoustofluidics 2: Perturbation theory and ultrasound resonance modes,” *Lab Chip* **12**(1), 20–28.
- Bruus, H. (2012b). “Acoustofluidics 7: The acoustic radiation force on small particles,” *Lab Chip* **12**(6), 1014–1021.
- Cai, H., Ao, Z., Wu, Z., Song, S., Mackie, K., and Guo, F. (2021). “Intelligent acoustofluidics enabled mini-bioreactors for human brain organoids,” *Lab Chip* **21**(11), 2194–2205.

- Carugo, D., Octon, T., Messaoudi, W., Fisher, A. L., Carboni, M., Harris, N. R., Hill, M., and Glynn-Jones, P. (2014). "A thin-reflector microfluidic resonator for continuous-flow concentration of microorganisms: A new approach to water quality analysis using acoustofluidics," *Lab Chip* **14**(19), 3830–3842.
- Ding, X., Peng, Z., Lin, S.-C. S., Geri, M., Li, S., Li, P., Chen, Y., Dao, M., Suresh, S., and Huang, T. J. (2014). "Cell separation using tilted-angle standing surface acoustic waves," *Proc. Natl. Acad. Sci. U.S.A.* **111**(36), 12992–12997.
- Dron, O., and Aider, J.-L. (2012). "Acoustic energy measurement for a standing acoustic wave in a micro-channel," *Europhys. Lett.* **97**(4), 44011.
- Dron, O., and Aider, J.-L. (2013). "Varying the agglomeration position of particles in a micro-channel using Acoustic Radiation Force beyond the resonance condition," *Ultrasonics* **53**(7), 1280–1287.
- Dron, O., Ratier, C., Hoyos, M., and Aider, J.-L. (2009). "Parametric study of acoustic focusing of particles in a micro-channel in the perspective to improve micro-PIV measurements," *Microfluid. Nanofluid.* **7**(6), 857–867.
- Dual, J., and Schwarz, T. (2012). "Acoustofluidics 3: Continuum mechanics for ultrasonic particle manipulation," *Lab Chip* **12**(2), 244–252.
- Dumy, G., Hoyos, M., and Aider, J.-L. (2019). "Observation of selective optical manipulation of particles in acoustic levitation," *J. Acoust. Soc. Am.* **146**(6), 4557–4568.
- Dumy, G., Jeger-Madiot, N., Benoit-Gonin, X., Mallouk, T. E., Hoyos, M., and Aider, J.-L. (2020). "Acoustic manipulation of dense nanorods in microgravity," *Microgravity Sci. Technol.* **32**(6), 1159–1174.
- Evander, M., and Nilsson, J. (2012). "Acoustofluidics 20: Applications in acoustic trapping," *Lab Chip* **12**(22), 4667–4676.
- Folds, D. L., and Loggins, C. D. (1977). "Transmission and reflection of ultrasonic waves in layered media," *J. Acoust. Soc. Am.* **62**(5), 1102–1109.
- Friend, J., and Yeo, L. Y. (2011). "Microscale acoustofluidics: Microfluidics driven via acoustics and ultrasonics," *Rev. Mod. Phys.* **83**(2), 647–704.
- Gorkov, L. (1962). "On the forces acting on a small particle in an acoustic field in an ideal fluid," *Sov. Phys. Dokl.* **6**, 773–775.
- Hagsäter, S. M., Jensen, T. G., Bruus, H., and Kutter, J. P. (2007). "Acoustic resonances in microfluidic chips: Full-image micro-PIV experiments and numerical simulations," *Lab Chip* **7**(10), 1336–1344.
- Hasegawa, T., and Yosioka, K. (1969). "Acoustic-radiation force on a solid elastic sphere," *J. Acoust. Soc. Am.* **46**, 1139–1143.
- Hawkes, J. J., and Coakley, W. T. (2001). "Force field particle filter, combining ultrasound standing waves and laminar flow," *Sens. Act. B: Chem.* **75**(3), 213–222.
- Hill, E. v. K., and Egle, D. M. (1980). "A reciprocity technique for estimating the diffuse-field sensitivity of piezoelectric transducers," *J. Acoust. Soc. Am.* **67**(2), 666–672.
- Hill, M., Shen, Y., and Hawkes, J. J. (2002). "Modelling of layered resonators for ultrasonic separation," *Ultrasonics* **40**(1-8), 385–392.
- Hultström, J., Manneberg, O., Dopf, K., Hertz, H., Brismar, H., and Wiklund, M. (2007). "Proliferation and viability of adherent cells manipulated by standing-wave ultrasound in a microfluidic chip," *Ultrasound Med. Biol.* **33**(1), 145–151.
- Jeger-Madiot, N., Arakelian, L., Setterblad, N., Bruneval, P., Hoyos, M., Larghero, J., and Aider, J.-L. (2021). "Self-organization and culture of Mesenchymal Stem Cell spheroids in acoustic levitation," *Sci. Rep.* **11**(1), 8355.
- Kandemir, M., Beelen, M., Wagterveld, R., Yntema, D., and Keesman, K. (2021). "Dynamic acoustic fields for size selective particle separation on centimeter scale," *J. Sound Vib.* **490**, 115723.
- Karlsen, J. T., and Bruus, H. (2015). "Forces acting on a small particle in an acoustical field in a thermoviscous fluid," *Phys. Rev. E* **92**(4), 043010.
- King, L. V. (1934). "On the acoustic radiation pressure on spheres," *Proc. R. Soc. London, Ser. A: Math. Phys. Sci.* **147**(861), 212–240.
- Laurell, T., Petersson, F., and Nilsson, A. (2007). "Chip integrated strategies for acoustic separation and manipulation of cells and particles," *Chem. Soc. Rev.* **36**(3), 492–506.
- Lenhof, A., Magnusson, C., and Laurell, T. (2012). "Acoustofluidics 8: Applications of acoustophoresis in continuous flow microsystems," *Lab Chip* **12**(7), 1210–1223.
- Luo, X., Cao, J., Gong, H., Yan, H., and He, L. (2018). "Phase separation technology based on ultrasonic standing waves: A review," *Ultrason. Sonochem.* **48**, 287–298.
- Miura, Y., Li, M.-Y., Birey, F., Ikeda, K., Revah, O., Thete, M. V., Park, J.-Y., Puno, A., Lee, S. H., Porteus, M. H., and Paşca, S. P. (2020). "Generation of human striatal organoids and cortico-striatal assembloids from human pluripotent stem cells," *Nat. Biotechnol.* **38**(12), 1421–1430.
- Nordin, M., and Laurell, T. (2012). "Two-hundredfold volume concentration of dilute cell and particle suspensions using chip integrated multi-stage acoustophoresis," *Lab Chip* **12**(22), 4610–4616.
- Petersson, F., Åberg, L., Swärd-Nilsson, A.-M., and Laurell, T. (2007). "Free flow acoustophoresis: Microfluidic-based mode of particle and cell separation," *Anal. Chem.* **79**(14), 5117–5123.
- Royer, D., and Dieulesaint, E. (1999). *Elastic Waves in Solids I: Free and Guided Propagation* (Springer Science & Business Media, New York).
- Settnes, M., and Bruus, H. (2012). "Forces acting on a small particle in an acoustical field in a viscous fluid," *Phys. Rev. E* **85**(1), 016327.
- Thielicke, W. (2014). "The flapping flight of birds: Analysis and application," Ph.D. thesis, University of Groningen, Groningen, the Netherlands.
- Thielicke, W., and Stamhuis, E. J. (2014). "PIVlab—Towards user-friendly, affordable and accurate digital particle image velocimetry in MATLAB," *J. Open Res. Softw.* **2**, e30.
- Vitali, V., Core, G., Garofalo, F., Laurell, T., and Lenhof, A. (2019). "Differential impedance spectra analysis reveals optimal actuation frequency in bulk mode acoustophoresis," *Sci. Rep.* **9**(1), 1–10.
- Widener, M. W. (1980). "The measurement of transducer efficiency using self-reciprocity techniques," *J. Acoust. Soc. Am.* **67**(3), 1058–1060.
- Wiklund, M. (2012). "Acoustofluidics 12: Biocompatibility and cell viability in microfluidic acoustic resonators," *Lab Chip* **12**(11), 2018–2028.
- Wiklund, M., Green, R., and Ohlin, M. (2012). "Acoustofluidics 14: Applications of acoustic streaming in microfluidic devices," *Lab Chip* **12**(14), 2438–2451.
- Wiklund, M., Toivonen, J., Tirri, M., Hänninen, P., and Hertz, H. M. (2004). "Ultrasonic enrichment of microspheres for ultrasensitive biomedical analysis in confocal laser-scanning fluorescence detection," *J. Appl. Phys.* **96**(2), 1242–1248.
- Wu, M., Ozcelik, A., Rufo, J., Wang, Z., Fang, R., and Jun Huang, T. (2019). "Acoustofluidic separation of cells and particles," *Microsyst. Nanoeng.* **5**(1), 32.
- Zhang, S., Kube, C. M., Song, Y., and Li, X. (2016). "A self-reciprocity calibration method for broadband focused transducers," *J. Acoust. Soc. Am.* **140**(3), EL236–EL241.